Determine the coordination of Al and Si of Fe-rich fly ash: The challenge in NMR and how we probe its heterogeneity using X-ray spectromicroscopy

Jiaqi Li [a,*], Ke Xu [b], Guoqing Geng [c], Harris E. Mason [a,d]

[a] *Atmospheric, Earth, and Energy Division, Lawrence Livermore National Laboratory, United States*
[b] *Department of Civil and Environmental Engineering, University of California, Berkeley, United States*
[c] *Department of Civil and Environmental Engineering, National University of Singapore, Singapore*
[d] *Center for National Security Applications of Magnetic Resonance, Lawrence Livermore National Laboratory, United States*

ARTICLE INFO

ABSTRACT

Scanning transmission X-ray microscopy (STXM) coupled with ptychographic imaging at Al and Si K-edge is a new probe to the microscale chemistry of heterogenous materials. Here, the combined techniques are applied to study local coordination environment of Fe-rich fly ash (FA). Ptychographic imaging at Al K- and Si K-edge highlights the fine Al- and Si-rich morphological features, respectively, at 6 nm pixel resolution. STXM visualizes the inter- and intra-particle variations in the silicate polymerization degree and two types of Al coordination environment in FA. The Si K-edge of SiO_4 connected with four-fold coordinated Al is higher than SiO_4 sharing oxygen with six-fold coordinated Al. The result is consistent with bulk nuclear magnetic resonance spectroscopy measurement of the Fe-rich sample which, however, is sensitive to paramagnetic Fe and time-consuming. We demonstrate that the combined method has great potential in the studies of chemically heterogenous aluminosilicates.

1. Introduction

Portland cement production, ~4.1 billion metric tons per year, contributes to 8 % of global anthropogenic CO_2 emissions [1]. The partial replacement of Portland cement clinker with supplementary cementitious materials (SCMs, e.g., industrial byproducts, calcined clay, and limestone) is the most mature strategy to lower the carbon footprint of cement and concrete [2–4]. Coal fly ash (FA), a byproduct from coal-fired power plants, is the most commonly used SCM due to its massive co-production, 700–1000 million metric tons (Mt) per year [3]. However, only 330–400 Mt./year of FA is used as SCMs due to its carbon content, low reactivity, and variation in quality. FA typically can only substitute up to ~35 wt% of clinker. In addition, FA is the precursor of alkali-activated materials, a type of low-carbon binder [5]. Understanding the structure of FA is critical to improving its reactivity and optimizing its use in low-carbon cement-based materials, alkali-activated materials, and geological carbon storage [6].

The ASTM C618 standard [7] limits minimum (SiO_2 + Al_2O_3+ Fe_2O_3) content of 50 wt% for the bulk compositions of both Class F and Class C FA. Class F has a maximum CaO content 18 wt% while the CaO content of Class F is >18 wt%. Ca-rich Class C is typically more reactive but more chemically heterogeneous relative to Class F. Thus, Class C FA is frequently rejected and less utilized in concrete [8]. Appropriate characterization of heterogeneous FA is needed for improving the understanding of its structure and for optimizing its utilization in concrete [3].

Conventional characterization of FA relies on X-ray diffraction (XRD), X-ray fluorescence (XRF) [9], and nuclear magnetic resonance (NMR) spectroscopy [10–11] to quantify crystalline phases, chemical compositions, and coordination environment of bulk samples. The use of NMR for FA characterization can be problematic when samples are Fe-rich. Paramagnetic ions clearly cause line-broadening of NMR resonances, lowering the accuracy of peak deconvolution of NMR spectra [12]. Moreover, the variation among FA spheres cannot be spatially distinguished by these techniques. Micro-XRD can be used to quantify crystalline phases of FA [13] but is incapable of providing useful information of glass phases of FA. Micro-XRF [14] and scanning electron microscopy-energy-dispersive X-ray spectroscopy (SEM-EDS) [8] can probe the local variation in FA chemical compositions. However, the spatial variation in the Al and Si coordination environments of glass, the majority of FA, cannot be determined using the aforementioned techniques.

---

* Corresponding author.
  E-mail address: li88@llnl.gov (J. Li).

FA is Al- and Si-rich and contains four-fold coordinated Al (Al[IV]), six-fold coordinated Al (Al[VI]), and four-fold coordinated Si [15]. It remains unclear how different Al species distribute and how Al correlates to silicate polymerization in FA glass. A reliable technique that probes the local coordination environment, especially Al and Si, of FA is needed. Scanning transmission X-ray miscopy (STXM) is a powerful tool to probe the coordination environment of phases in the form of X-ray absorption near-edge fine structure (XANES) spectra with submicron spatial resolution (25–60 nm). STXM has been successfully applied to study the hydration of cement phases (dicalcium silicate [16], tricalcium silicate [17], calcium aluminate [18], tricalcium aluminate [19]) and the local coordination environment of their reaction products [20–23]. STXM can be further extended to probe the heterogeneity of FA and its Al and Si coordination environment.

The spatial resolution of STXM is effectively limited by the size of the zone plate in STXM. Thus, the very fine morphological features with coordination environment information of cement-related materials, e.g., internal structure of FA, may not be unveiled using STXM [24]. Ptychography is an advanced scanning-based coherent diffractive imaging technique that provide images with spatial resolution finer than the zone plate of STXM, the limiting factor of STXM spatial resolution. In recent ptychography studies of materials, including cement-related materials, mostly images were taken in the energy ranges of 600–1000 eV [16,18,23] or 4000–12,000 eV [25,26], instead of 1300–1900 eV, due to the instrumental limitations. Soft X-ray ptychography allows pixel resolution down to ~4 nm while the penetration depth can be just few microns, which seems not an issue for mesoporous cement hydrates (e. g., calcium silicate hydrate) [16]. However, the X-ray beam in such a low energy range cannot penetrate larger solid fly ash spheres. The beam in the tender-to-hard X-ray range allows much larger penetration depth (i.e., larger samples) but commonly provides a lower spatial resolution, e.g., ~30 nm or coarser, which limits users to probe the fine structure of FA particles. Moreover, both energy ranges cannot excite Al or Si, the major elements of interest, in FA because their K-edge energies are 1500–1850 eV. Transmission electron microscopy (TEM) coupled with electron energy loss spectroscopy can potentially map the Si coordination environments, but the Al coordination mapping can be limited by emission artifact Schottky emitters [27]. Moreover, the electron penetration depth through cement-related materials in TEM is typically just hundreds of nanometers, insufficient to large solid FA spheres. Thus, STXM with ptychographic imaging at Al- and Si K-edge with high spatial resolution could be an ideal tool to study the local distribution of different coordination environments of Al and Si of cement-related materials, such as FA.

This article presents a new combined experimental method that separates and visualizes different coordination environments of Al and Si in fly ash. X-ray ptychography imaging at K-edge energy highlights the fine morphological features of elements of interest (i.e., Al and Si) at the pixel resolution of 6 nm. Scanning transmission X-ray microscopy distinguishes inter- and intra-particle spatial variations in silicate polymerization degree and coordination number of Al (four- and six-) in the form of X-ray absorption near-edge structure spectra. Our X-ray spectromicroscopic results exhibit great potential in the use of this combined method in fly ash-related studies and studies of other poorly crystalline or glassy aluminosilicate materials (e.g., volcanic ash). Through the comparison with ^{27}Al and ^{29}Si NMR experiments, we demonstrated the instrumental advantage of STXM in terms of probing Al and Si coordination environments of heterogenous aluminosilicate for paramagnetic-element-rich samples.

2. Material and methods

2.1. Material

Class C FA with 83.2 wt% amorphous content was studied. The FA chemical compositions are listed in Table 1. Other physical and chemical properties of the sample can be found in [28]. The FA sample contains no crystalline silicate or aluminate phases with the exception of ~9 wt% quartz. FA was dispersed in 100 % ethanol with a liquid to solid mass ratio of 100. The sample was then drop-cast on a carbon-film TEM grid (Ted Pella). The well dispersed drop-cast sample has a thickness below 10 μm. Over-dose of fly ash particles on a TEM grid would result in X-ray absorption saturation in agglomerated areas.

2.2. Methods

2.2.1. STXM and ptychography

STXM images and XANES spectra were collected at the beamline 7.0.1.2 (COSMIC) at the Advanced Light Source (ALS), the Lawrence Berkeley National Laboratory. The STXM beamline uses a monochromatic synchrotron X-ray source. More details regarding the microscope configuration can be found in [29]. Each STXM measurement was taken for a stack of images collected at a single X-ray photon energy. Each STXM image consists of pixels (45 nm resolution) corresponding to the intensity of transmitted photons at each energy. By collecting images at each energy step around an absorption edge (e.g., Al K-edge), the image stack can be coded into an [x, y, I_T] matrix, where x and y correspond to the pixel position in a region of interest (ROI), and I_T corresponds to the transmitted photon intensity in the pixel at a given energy. Image stacks were taken around Al K-edge and Si K-edge with an energy resolution of 0.1 eV.

The absorption pixels at the defined energy range were then processed using K-Means clustering algorithm to group a set of XANES spectra, where each spectrum X_i is a vector of absorption features (e.g., peak position, intensity, and width) [30–32]. K-Means is a widely used iterative algorithm that tries to partition the dataset into K pre-defined disjoint clusters [33–35]. In this research, the number groups of spectra (k) was pre-set based on the pre-knowledge of the fly ash sample and each XANES spectrum X_i were randomly assigned (random partition) a cluster label $y_i \in [1, k]$ using pySTXM, a python-based data collection and graphical user interface package [36]. Then, two steps were conducted iteratively until reaching the maximum steps or the change of clusters is very minor:

(1) y_i is fixed; update the mean of cluster i: $\mu_i = \frac{1}{n_i} \sum_{y_j = i} X_j$

(2) μ_i is fixed; update the label of each spectrum X_j by finding y_j that minimizes: $\sum_{i=1}^{k} \sum_{y_j = i} |X_j - \mu_i|^2$

The absolute intensity (I_A) of optical density of each XANES spectrum at each energy step is converted as Eq. (1) [20].

$$I_A = ln\left(\frac{I_I}{I_T}\right) \tag{1}$$

where I_I is the incident X-ray photon intensity, which is about equivalent to the I_T of a sample-free area (purely carbon-film of the TEM grid). Thus, I_A of a sample-free area is nearly 0. I_A at K-edge energy is a useful estimated index for the content of element of interests (i.e., Al and Si in

Table 1
Oxide composition (wt%) of FA.

SiO$_2$	Al$_2$O$_3$	Fe$_2$O$_3$	CaO	MgO	SO$_3$	Na$_2$O	K$_2$O	TiO$_2$	P$_2$O$_5$	LOI
38.7	18.9	6.6	22.9	4.0	1.0	2.1	0.5	1.2	2.2	0.4

this study) at each pixel [37]. Higher I_A at the K-edge energy indicates a higher Al or Si content. Higher I_A at a pre-edge energy (1540 eV for Al and 1815 eV for Si) indicates a higher optical density for background, i. e., a denser and/or thicker area on a pixel. The absolute intensity ratio is expressed as the maximum I_A at the K-edge divided by the minimum I_A at pre-edge energy (1540 eV for Al and 1815 eV for Si). Thus, this intensity ratio can be used to qualitatively estimate the Al and Si concentration at each pixel [38]. I_A of each XANES spectrum can be linearly normalized with the [0,1] function. Where the minimum normalized intensity (I_N) at the pre-edge energy (1540 eV for Al and 1815 eV for Si) is defined as 0. The maximum value of I_A, at the K-edge energy, is normalized to 1 for I_N. I_N is useful for differentiating Al and Si species of a XANES spectrum at each pixel in analytic programs, e.g., pySTXM.

The normalized XANES spectra of this fly ash sample grouped by the K-Means clustering algorithm were outputted from pySTXM and used as inputs (i.e., reference spectra) in aXis2000 [39], a commonly used STXM analysis software. Note that these references spectra were obtained from the FA sample itself, not from existing literature. See the Results and Discussion Section for the reference examples of XANES spectra in this study. RGB overlay maps were created using aXis2000 to visualize various coordination environments. The RGB overlay maps were plotted in the principal components space based on the singular value decomposition (SVD) method with above-mentioned reference XANES spectra of this FA sample. For the singular value decomposition, the cluster (group) of spectra can be decomposed by $X = UDV^T$ with the number of spectra is larger than the number of absorption features [40]. Based on the principal components analysis (PCA) theory [41], the eigenvectors V calculated from the SVD are the eigenvectors of X^TX, which is what we need for PCA, because $X^TX = VD^TU^TUDV^T = VD^2V^T$ [40]. To project the spectra to the principal components space, which maximizes variance of projected data, we project the spectra to the coordinate (vector) V_1 of the eigenvectors V [42].

X-ray ptychographic images (6 nm pixel resolution) were collected at the Al K-edge and Si K-edge using the STXM setup but with a far-field CCD camera [43]. Diffraction patterns were collected using the camera in 60 nm increments to ensure overlap of the scanned areas and reconstructed using a GPU-based ptychography reconstruction algorithm [29]. All ptychographic images were exported using pySTXM. Over 200 FA grains on the TEM grid were measured at room temperature in vacuum.

2.2.2. NMR

The ^{27}Al and ^{29}Si single pulse magic angle spinning nuclear magnetic resonance (SP/MAS NMR) spectra were collected on a 400 MHz Bruker Avance III spectrometer using a triple resonance Bruker probe configured for 4 mm (outer diameter) rotors. Both spectra were collected at a spinning rate of 14 kHz. The ^{27}Al spectrum was collected using a 1.5 μs pulse (corresponding to a 27° tip angle) using a 0.5 s pulse delay for 2048 scans and referenced to an external solution of 0.1 M Al(NO₃)₃ (δAl = 0 ppm). The ^{29}Si spectrum was collected using a 5.0 μ 90° pulse using a 8 s pulse delay for 7767 scans and referenced to a solid sample of kaolinite (δSi = −92 ppm [44]). Multiple quantum (MQ) NMR spectra were collected using both the standard z-filtered MQ/MAS sequence [45] as well as that using a split-t1 acquisition with a double frequency sweep reconversion for full echo acquisition without need to perform a shearing transform [46]. With full echo acquisition, the later sequence was used as a filter to remove components with short T_2 relaxation times. Spectral fitting was performed using the dmfit software [47]. ^{27}Al parameters were derived from direct fitting of the 2D MQ/MAS data in dmfit. We performed an error analysis on the ^{29}Si NMR data using the built in Monte Carlo error estimator in the dmfit software. A total of 400 iterations were used, and the errors presented as the 1σ standard deviation. Due to the computationally intense nature of the MQ/MAS fitting a similar error analysis of this data was not feasible.

3. Results and discussions

3.1. XANES and ptychography imaging

The absorption ptychographic images Fig. 1a and b show different morphological features of FA excited at Al K-edge (1555 eV) and Si K-edge (1821.5 eV), respectively, in the ROI. Compared to Fig. 1b, the largest particle (plerosphere) in Fig. 1a exhibits many fine globular features, suggesting the Al-rich but Si-poor inclusion (i.e., sub-spheres) encapsulated in the plerosphere in Fig. 1a and few Si-rich sub-spheres in Fig. 1b. Apparently, FA particles in the whole area exhibit different detailed morphologies. The lower-left solid FA sphere contains at least three cavities.

Fig. 1c shows three representative Al K-edge XANES spectra (normalized intensity) obtained from the ROI using the K-Means clustering analysis described in the Method section. These references spectra are from this FA sample, not from existing literature. The pre-edge weak shoulder A of the Al K-edge XANES spectra in Fig. 1c corresponds to the dipole-forbidden transition from 1s to 3s electrons of Al [48]. The major peak C^{IV} or C^{VI} (Al K-edge) is attributed to the allowed electron transition of 1s to antibonding states (3p orbital) of Al. Post-edge peaks E and G are the results of electron transitions from 1s to 3d orbitals of Al. Based on the SVD method, the red, green, and blue spectra in Fig. 1c were used as reference spectra to plot the red, green, blue in Fig. 1d RGB overlay map, respectively. Compared to Fig. 1d, the ptychographic image Fig. 1a is much sharper with clearer enhanced edge and more details of morphological features due to the higher spatial resolution of ptychography. The grain boundaries of the sub-spheres of the largest particle and voids in the lower-left sphere were not clearly observed in Fig. 1d STXM RGB overlay map. Note that, the ptychographic imaging at Al K- and Si K-edge is a significant advance in instrumental development compared to imaging at 800 eV in a previous study [18] because beam at 800 eV cannot excite electron transitions of the elements of interest (e.g., Al and Si) of FA.

Minor elements as the second-nearest neighbor of Al atom affect the K-edge energy of glassy materials [49,50,51]. Phase identification of a disordered material with various complex compositions might be impossible and meaningless because only few peaks or shoulders can be used as fingerprints for phase identification. However, the peak energy of Al K-edge still provides valuable chemical information to differentiate environments of four- and six-fold coordinated Al. The K-edge energy of six-fold coordinated Al is typically 2–3 eV higher than that of four-fold coordinated Al [48]. The major peak C^{IV} of the red spectrum at ~1547.9 eV in Fig. 1c suggests four-fold coordinated Al (Al[IV]) in the red region in Fig. 1d. This Al[IV] constitutes the Q^4(mAl) glass of FA as a network former. The peak C^{VI} of the green spectrum at ~1550.4 eV is positioned at 2.5 eV higher energy than that of the red spectrum. Such a high peak energy represents six-fold coordinated Al (Al[VI]) [48] and the presence of a Al[IV] shoulder at ~1547.1 eV both suggest a mullite-like Al coordination environment (a mixture of Al[IV] and Al[VI]) in the green region in Fig. 1d [52,53] or a mixture of phases with both Al[IV] and Al[VI]. The green spectrum is comparable to mullite spectra in existing literature [52,53] (see Supplementary Information for the spectra of mullite and aluminosilicate glass). The broad peak C^{VI} at 1551.4 eV of the blue spectrum represents Al[VI] with a highly disordered local structure in calcium aluminosilicate glass with a broad range of chemical compositions in the blue region because calcium aluminosilicates with fixed chemical compositions presents spectra with well-resolved peaks and shoulders [50,54]. Compared to the green spectrum, the 1.1 eV higher energy of the Al K-edge of the blue one suggests a longer mean Al[VI]-O bond of the first coordination shell in the blue region (e.g., Al-rich sub-spheres in the plerosphere) with relatively low Si content [48,55]. The Al K-edge of calcium aluminosilicate increases as Si content decreases and Ca content increases [50]. The presence of both Al[IV] and Al[VI] in FA is consistent with ^{27}Al NMR studies [10,15]. The Al[VI] acts as a network modifier.
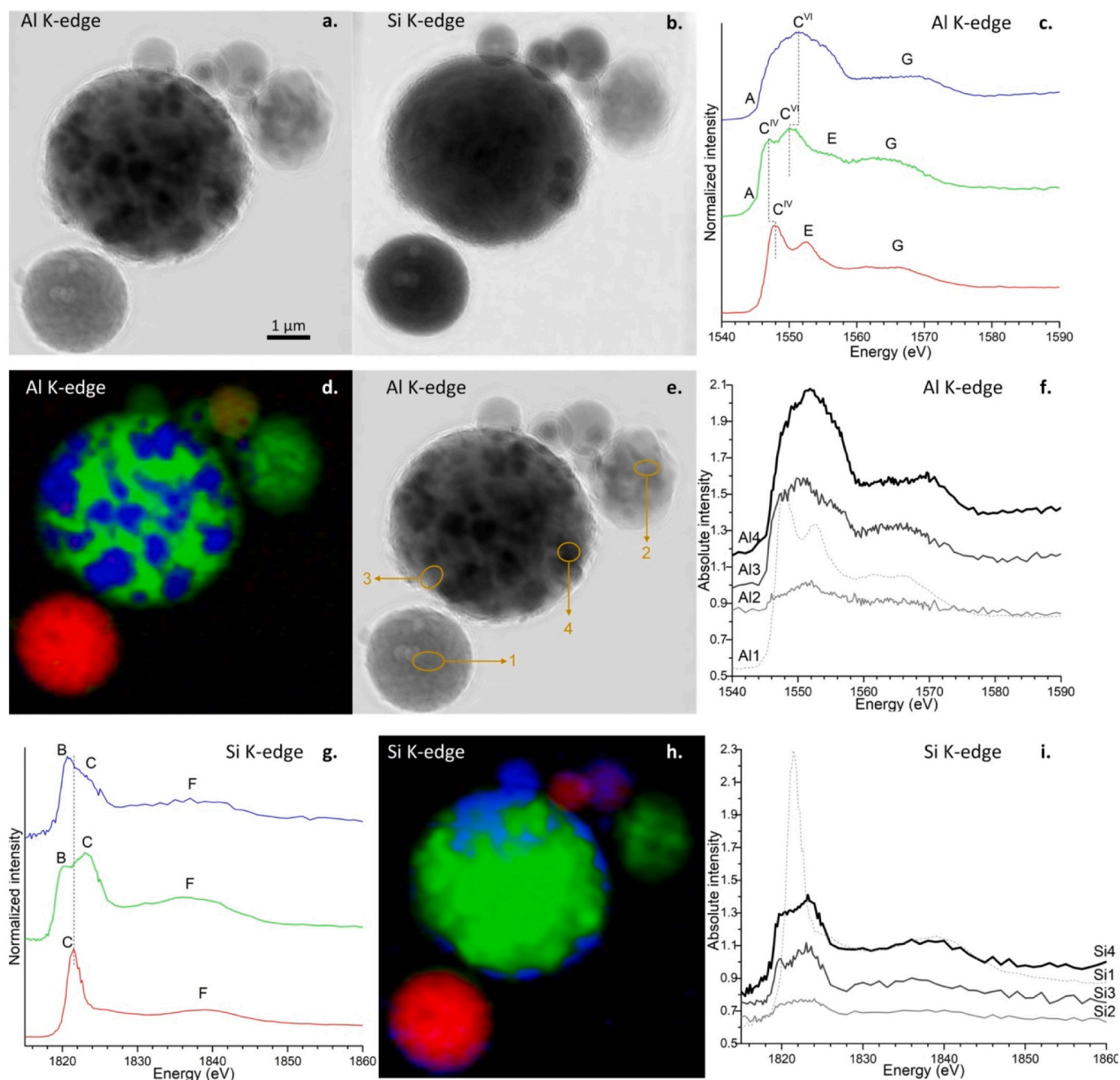
Fig. 1. (a) ptychographic magnitude image of the ROI taken at Al K-edge 1550.5 eV; (b) ptychographic magnitude image of the ROI taken at Si K-edge 1821.5 eV; (c) Al K-edge XANES spectra with normalized intensity extracted from K-Means clustering analysis; (d) Al RGB overlay map plotted with XANES spectra at Al K-edge obtained from (c) using the singular value decomposition method, red, green, blue regions were plotted with the red, green, and blue spectra in (c), respectively; (e) selected regions in the ptychographic image for plotting XANES spectra with absolute intensity in (f) and (i); (f) Al K-edge XANES spectra with absolute intensity extracted from four regions specified in (e), spectra Al1, Al2, Al3, and Al4 are extracted from regions 1, 2, 3, 4, respectively; (g) Si K-edge XANES spectra with normalized intensity extracted from K-Means clustering analysis; (h) Si RGB overlay map plotted with XANES spectra at Si K-edge obtained from (g) using the singular value decomposition method, red, green, blue regions were plotted with the red, green, and blue spectra in (g), respectively; (i) Si K-edge XANES spectra with absolute intensity extracted from four regions specified in (e), spectra Si1, Si2, Si3, and Si4 are extracted from regions 1, 2, 3, 4, respectively. The sub-spheres are Fe-bearing validated by Fe L$_{2,3}$-edge XANES, which are not shown because 1) all Fe L$_{2,3}$-edge XANES spectra here are nearly identical, and 2) Fe L$_{2,3}$-edge is only sensitive to Fe oxidation degree.

The Al coordination environments between and within the spheres are heterogeneous. The lower-left solid sphere in Fig. 1d is purely red, suggesting the presence of only one type of Al species, Al[IV], while other spheres mainly intermix with two colors, meaning at least two types of Al coordination environments. The sub-spheres and the matrix of the plerosphere exhibit two different types of Al coordination environment: green (mullite-like Al[IV] and Al[VI]) and blue (highly disordered Al[VI]), respectively. The Al K-edge XANES spectra with absolute intensity in Fig. 1f are extracted from regions specified in Fig. 1e. The absolute intensity at K-edge suggests the content of an element of interest while the absolute intensity at pre-edge (e.g., 1540 eV) suggests the optical density. Thus, the intensity ratio at the K-edge over the pre-edge (the highest absolute intensity over the lowest absolute intensity) suggests the concentration of an element of interest. The

high absolute intensity of the Al2 and Al3 spectra at pre-edge (e.g., 1540 eV) in Fig. 1f confirms the high optical density (i.e., the presence of heavier elements) of the green region in Fig. 1e. The absolute absorption intensity in Fig. 1f at Al K-edge peak is disproportional to that at pre-edge (e.g., 1540 eV), suggesting different Al concentrations in the four regions specified in Fig. 1e. The absolute intensity ratio at the Al K-edge over the pre-edge of the Al1 spectrum is ~3, much higher than that of the Al2, ~1.1. The different intensity ratios suggest the intra- and inter-particle spatial variations in Al concentration. The lower-left solid sphere exhibits a higher Al concentration than the rightmost one and the plerosphere matrix. Many sub-spheres in the plerosphere are more Al-rich than the plerosphere matrix. This variation in Al concentration of FA agrees with SEM-EDS and micro-tomography studies [8,56]. The lower-left solid sphere does not exhibit any variation in peak position or width, suggesting a homogenous Al coordination environment within the sphere.

The representative Si K-edge XANES spectra (normalized intensity) in Fig. 1g are also obtained from the ROI using the K-Means clustering analysis. The shoulder/peak B (Si K-edge) corresponds to the allowed electron transition of 1s to antibonding states (3p orbital) of Si atoms which partially share oxygen with Al[VI] of aluminosilicate glass [57]. The shoulder/peak C (Si K-edge) is also attributed to the 1s-3p electron transition of Si atoms, but partially share oxygen with Al[IV] [58]. The Si K-edge energy is sensitive to the degree of silicate polymerization and the second-nearest atom to Si [59]. The post-edge diffuse peak F is assigned to the electron transition from 1s to t_2 state. The lack of additional absorption features (peaks and shoulder) in the Si XANES spectra suggests that the Si in the sample is largely disordered. Otherwise, this Ca- and Al-bearing sample would exhibit many post-edge shoulders and peaks, as found in our calcium (alumino)silicates XANES database, see [59]. Fig. 1h shows the RGB overlay map at Si K-edge of the ROI based on three XANES reference spectra in Fig. 1g using the SVD method described in the Methods section. The red, green, and blue regions in Fig. 1h RGB overlay map contains Si as presented in red, green, and blue XANES spectra, respectively, of Fig. 1g. The intra- and inter-particle heterogeneity with respect to the Si coordination environment was observed. The lower-left sphere is almost purely red, while other spheres mainly intermix with two colors (i.e., at least two types of Si coordination environments).

Minor elements as the second-nearest neighbor of Si also affect the Si K-edge energy of glassy materials [51]. Glassy silicates only exhibit few peaks and shoulders in XANES spectra, making fingerprint phase identification challenging. As the degree of silicate polymerization increases with an increasing Si K-edge energy [59], the extracted XANES spectra still provide valuable chemical information. The peak C of the red spectrum is positioned at 1821.5 eV, ~1.5 eV lower than that of the green spectrum due to the weaker electron shielding of Si in the red region. The Si K-edge peak energy difference suggests 1) the presence of glass network modifiers (e.g., Na, K, and Ca) that balanced with Al in the red region, and 2) the presence of large second coordination shell atoms (e.g., Ti and/or Fe) as network formers in the green region [59,60,61,62]. Si K-edge energy increases with decreasing content of glass network modifiers and increasing content of large network formers. The peak of the red spectrum is sharper than that of the other two spectra, suggesting more ordered Si coordination with a larger Si cluster size in the red region relative to the other regions [63]. The Si ordering results are consistent with the fact that the green and blue regions mainly contain Si sharing oxygen with highly disordered Al and Al with two coordination environments (i.e., Al[IV] and Al[VI]). The peak B energy at 1820.9 eV of the blue spectrum is higher than the green counterpart, 1820.3 eV, suggesting a higher Si-O-Si/Al bond strength and/or a smaller Si-O-Si/Al bond angle in the blue region. The Si K-edge XANES spectra (not shown here) within the lower-left solid sphere have comparable peak position and width, suggesting a homogenous Si coordination environment within this sphere. The presence of different Si coordination environments in XANES spectra of the FA particles agrees

with ^{29}Si NMR studies, where the peaks in NMR spectra are very diffuse [10].

The color-mismatch between the two RGB overlay maps (Al K-edge in Fig. 1d and Si K-edge in Fig. 1f) with respect to the plerosphere suggests the heterogeneity of FA coordination chemistry and the Si-poor nature of many fine inclusions (i.e., sub-spheres). This fact is consistent with the results of the ptychography images (Fig. 1a and b). The majority of the sub-spheres is suggested to be Fe/Ca-Al oxide with relatively low Si content, which is consistent with micro-tomography and TEM studies [56,64]. The Si K-edge XANES spectra with absolute intensity in Fig. 1i are also extracted from areas specified in Fig. 1e. The absolute absorption intensity in Fig. 1i at the Si K-edge is also disproportional to that at pre-edge (e.g., 1815 eV), exhibiting the intra- and inter-particle variations in Si concentration of the FA sample. The lower-left solid sphere with homogenous Si concentration exhibits higher Si concentration than other particles in Fig. 1 h. The low absolute intensity ratio for both Al and Si in area2 in Fig. 1e suggests its low content of Al and Si, thus high content of other elements (i.e., very likely Ca-rich).

Fig. 2 shows the Al K- and Si K-edge energies of all measured particles in the FA sample. The scatters fall into three regions, α, β, and γ. Region α indicates silicate tetrahedra that mainly connect to Al[VI]. A positive correlation between Al K-edge and Si K-edge energies is found in region α. The Al K-edge energy of Al[VI] increases as the mean Al—O bond length increases [55]. The long Al[VI]-O bond and the low bond valence of Al[VI] with a high degree of local distortion correspond result in a higher Si K-edge energy of aluminosilicate glass [50]. Region β indicates silicate tetrahedra that mainly network with aluminate tetrahedra. Al [IV] acts as a network former and increases the network polymerization degree relative to the counterpart with network modifiers Al[VI]. The higher degree of network polymerization explains the higher Si K-edge energy in region β. The correlation between Al K- and Si K-edge energies in β is less pronounced due to the low variation in intertetrahedral Al-O-Si angles [65]. Region γ indicates heavy elements (e.g., Ti and Fe) incorporated in the aluminosilicate glass networks of FA [66]. As the heavy elements content of the FA is low, only several scatters are plotted here.

The present study demonstrates the intra- and inter-particle heterogeneity of Al and Si coordination environments of FA. The chemical heterogeneity (e.g., the spatial distribution of network modifiers and formers) affects the depolymerization of FA glass during pozzolanic reaction or alkali-activation. Thus, intra- and inter-particle variations in the reaction rate are inevitable in FA-based cementitious materials. In the studies of the pozzolanic reaction and alkali-activated materials using micro-analysis tools (e.g., SEM-EDS, TEM, micro-tomography,
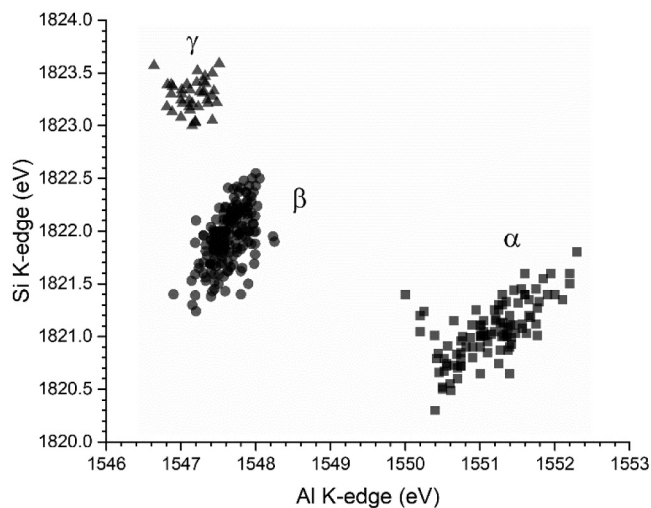

Fig. 2. Correlation between Al K-edge and Si K-edge of XANES spectra of the FA.

micro-Raman, micro-XRF, micro-XRD), statistically representative data of FA-based cementitious samples must be collected to support one's statement. An example of an inappropriate characterization of FA-based samples can be found in [67], where only one FA particle in each group of samples was measured by TEM to unveil the influences of different curing methods on the properties of high-volume FA concrete.

3.2. NMR

Our ^{27}Al NMR results in Fig. 3 indicate that three distinct Al environments can be identified in the FA material. However, these determinations are challenging and require effort beyond the standard solid-state NMR tools applied by cement chemists. Direct ^{27}Al SP/MAS NMR is insufficient to resolve chemical information about this material. Spectra collected at different magnetic field strengths and spinning rates show a broad and poorly resolved peak centered at 50 to 60 ppm that spans the entire range of chemical shifts expected for cement materials (Fig. 3). A small peak appears as a shoulder near 0 ppm but is completely obscured by the main peak. A spinning rate of 30 kHz was required to sufficiently prevent sideband overlap with the centerband but was still insufficient to resolve this additional peak. We also note that the increase in magnetic field strength from 9.4 to 14.1 T has a marginal effect on the spectral resolution and is likely due to paramagnetic broadening increasing with field strength while the quadrupole broadening decreases.

We relied on two different ^{27}Al MQ/MAS data sets for full spectral assignment in this system. The standard MQ/MAS experiment produced a broad and complex spectrum with multiple potential overlapping environments present that cannot be deconvolved easily. A second experiment collected using a split-t1 acquisition produced a cleaner spectrum is presented where a single peak from Al[IV] and that from Al[VI] can be observed. This peak is clearly present in the standard MQ/MAS spectrum (Fig. 4) but is obscured by the strong peak on the chemical shift axis (CS). This peak also completely obscures that of the Al[VI] near 0 ppm. Thus, this second data set acts as a spectral editing tool which retains some but not all of the Al environments and enhances signal from the Al[VI] peak. With the separation of these three peaks, they can be assigned to distinct phases in the FA material (Table 2). We assign the lone Al[VI] peak at $\delta_{iso} = 7.11$ ppm to that contained in mullite. The peak at $\delta_{iso} = 58.6$ ppm exhibits a small P_Q and is assigned

a.

b.

Fig. 4. ^{27}Al MQ/MAS spectra of the FA. (a) Data collected using the "standard" method with a zero-quantum filter; (b) Data collected using a double frequency sweep and a split-t1 acquisition.

to Al[IV] in a Ca-poor tectosilicate-like glass network. This assignment agrees with the chemical shift of Al[IV] in Ca-poor FA [68,10,11]. The large P_Q of 7.1 MHz observed for the final Al[IV] site combined with the average chemical shift of 74.1 ppm places this environment more in line with that for a disordered calcium aluminate phase (e.g., calcium dealuminate $\delta_{iso} = 75.5$ ppm and 69.5 ppm [69]) and/or disordered Ca-
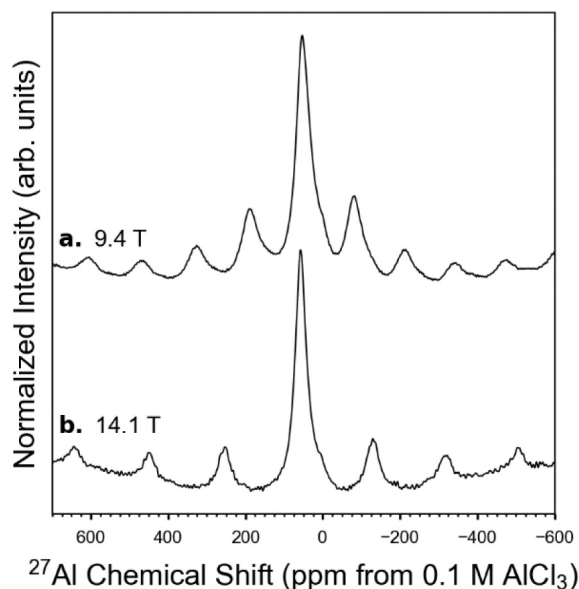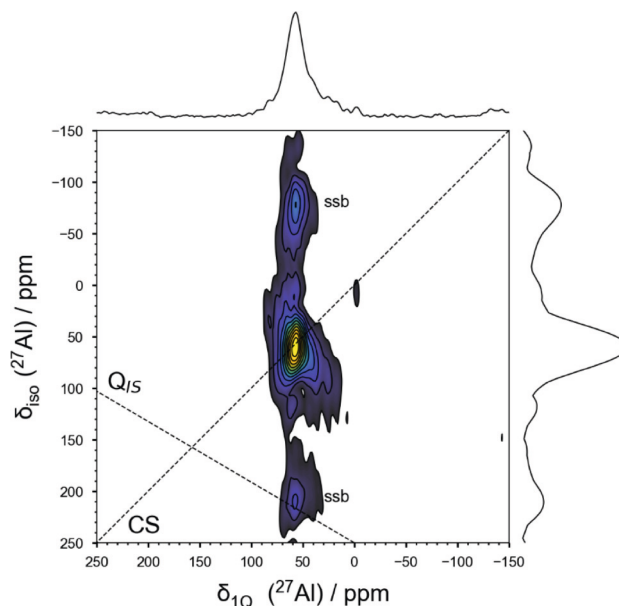

Fig. 3. ^{27}Al SP/MAS NMR spectra collected (a) at a 9.4 T magnetic field with a 14 kHz spinning rate and (b) at a 14.1 T magnetic field with a 30 kHz spinning rate.
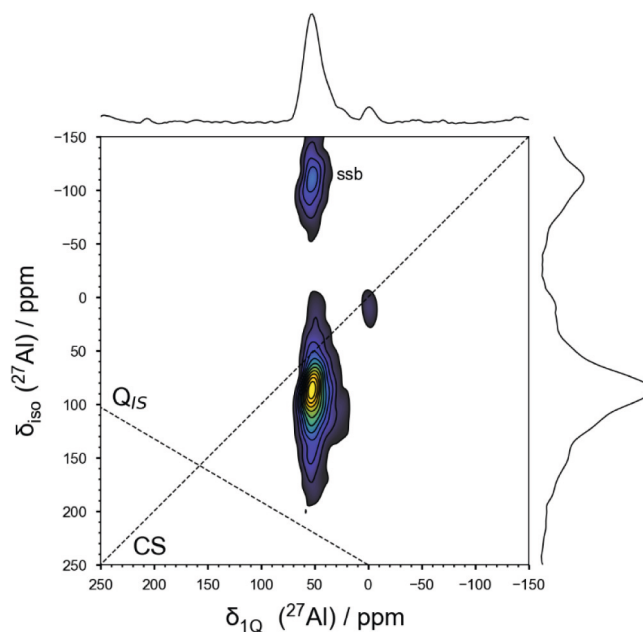
Table 2

Average ^{27}Al chemical shifts (δ_{iso}) and quadrupole products (P_Q) for the three Al sites in FA.

Site	δ_{iso} (ppm)	P_Q (MHz)
1	74.1	7.2
2	58.6	1.9
3	7.1	4.2

Table 3

Average spectral parameters derived from the ^{29}Si MAS/NMR data. Errors are presented as the 1σ standard deviation.

Site	δ_{iso} (ppm)	width (ppm)
1	−73.7 ± 0.1	6.8 ± 0.3
2	−91.0 ± 0.4	26.6 ± 0.7
3	−109.1 ± 0.4	17.5 ± 1.1
4	−126.4 ± 2.8	39.5 ± 3.8

rich aluminosilicate.

Comparison of our ^{29}Si data to those previously collected for FA reveals a similarly broad spectrum which is difficult to resolve the lineshape. Previous efforts have fit these spectral data with at times over 14 different Gaussian peaks which represent a severe overfitting of these data [70–72]. Barring more additional 2D NMR experiments [73], we have applied a conservative model with four main ^{29}Si NMR peaks were observed in Fig. 5. The two peaks at −91.2 and −109.2 ppm over the range for Q^3 and Q^4 species in the aluminosilicate network [15]. The peak at −73.7 ppm corresponds to isolated SiO_2 tetrahedra Q^0, indicating a small amount of merwinite [74,75], which is below the detection limit of XRD and out of our interest. The broad peak at −125.6 ppm is outside the normal range for silicates, possibly resulting from the paramagnetic interactions with Fe [76–80] (Table 3).

Our XANES results agree with our NMR results. Both Al[IV] and Al [VI] were found in this FA sample using the two techniques and Al[IV] is more abundant than Al[VI]. No Si-free-Al-rich spheres were observed in STXM, suggesting that the ^{27}Al NMR main peak at δ_{iso} = 74.1 ppm should be assigned to Ca-rich aluminoslicate, which stoichiometrically contains less Si compared to Ca-poor aluminosilicate and calcium silicate [8]. The largely scattered K-edge energies and the broad peaks of XANES spectra suggest the heterogeneous and disorder nature of Al and Si in FA, consistent with the broad peaks in ^{27}Al and ^{29}Si NMR. Although Si K-edge energy is sensitive to the degree of aluminosilicate polymerization, this degree cannot be quantified using XANES. ^{29}Si NMR is a powerful tool to determine this polymierization degree. However, for this Fe-rich FA sample, the quantification of degree of polymerization is challenging due to the paramagnetic interactions with Fe. Although NMR is a commercially available technique with a large database of Al

and Si chemical shifts and more accessible than STXM, we demonstrated that determining the coordination environment of Al and Si in a Fe-rich (6.6 wt% Fe_2O_3) FA sample using NMR is already challenging and time-consuming. The total data collection time of this NMR work is 17 h for ^{29}Si and a combined total of over 30 h for the ^{27}Al NMR study. NMR studies of SCMs with higher Fe content (e.g., FA with 21 wt% Fe_2O_3) could be even more challenging. STXM can be a highly efficient alternative to NMR for studying the coordination environments of Al and Si of cement-related materials.

3.3. Discussion

The dissolution reactivity of FA glassy phases largely relates to both the compositions and coordination environments of the glasses [3]. Ca, Mg, Na, potassium, and Al[VI] are network modifiers of FA glasses while Si and Al[IV] are major network formers. The glass reactivity negatively correlates to the degree of silicate polymerization. Ca-rich glasses exhibits a higher dissolution rate and pozzolanic reactivity relative to Si-rich glasses as Ca depolymerizes silicate networks [81]. Al as a network modifier also considerably increases the dissolution rate and pozzolanic reactivity of aluminosilicate glasses. The glass dissolution rate is also influenced by aqueous chemistry. Ca-rich alkaline solution promotes the precipitation of calcium silicate hydrate (C-S-H) on glass surfaces, and C-S-H acts as a barrier against further OH- and alkali ions diffusion towards glass and limiting further dissolution of glasses [82]. Al leached from glasses can reintegrate on glass surfaces, forming Ca-modified aluminosilicate layer with Al-O-Si species [83]. As the Si K-edge energy generally increases with an increasing degree of aluminosilicate polymerization, the high Si K-edge areas (the network former Al [IV]-rich regions β and γ in Fig. 2) of FA glass probed in this study indicate lower dissolution and pozzolanic reactivities. The Si K-edge of the glass with higher Ca content positions at a lower energy, indicating higher reactivities. The low Si K-edge area (the network modifier Al[VI]-rich region α in Fig. 2) with a relatively low degree of aluminosilicate polymerization indicates higher dissolution and pozzolanic reactivities. This heterogenous coordination environments of Al and Si of this FA sample suggests nonuniform reactivities in Ca-rich FA, consistent with previous SEM-EDS results of other FA samples [84,8].

To the best of the authors' knowledge, COSMIC is the only soft X-ray spectromicroscopic beamline that couples STXM with ptychography and is capable of sharp ptychographic imaging at the energy of 1500–1850 eV (in fifth harmonics) at spatial resolution <10 nm. Other ptychographic imaging microscopy at STXM/ptychography beamlines at other synchrotron facilities were mainly optimized at the energy range of 700–1000 eV (in third harmonics) due to the limitations of their beam brilliance, CCD detectors, microscopic configuration, or optimized algorithm [85–87]. Other X-ray absorption beamlines are primarily in the beam energy range of 2–12 keV or higher [88,25], which does not cover the K-edge of major elements of FA, e.g., O, Na, Mg, Al, and Si. Other soft X-ray STXM beamlines without the ptychographic imaging technique are only capable of probing absorption features at a spatial resolution down to ~30 nm, which may be insufficient to image the fine structure of FA. However, limitations of the application of COSMIC (STXM/pty-chography) beamline in SCM-related studies should not be ignored. The designed energy range of the COSMIC beamline is 250–2500 eV, below the K-edge energies of many heavy elements (e.g., potassium, Ca, Ti and
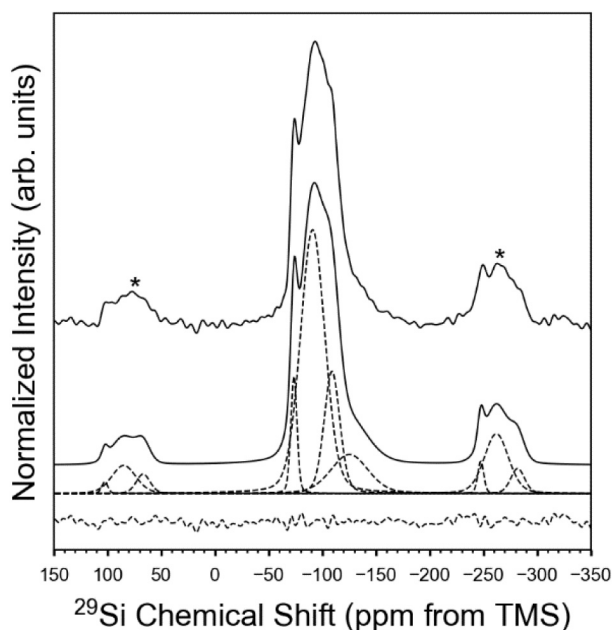

Fig. 5. ^{29}Si MAS NMR spectrum of the FA. The top spectrum is measured result, and the dashed peaks at the bottom are from its deconvolution. Fitted spectrum is the in-between. The difference between the data and the fit is presented at the bottom. * denotes the spinning sideband.

Fe), which may be interesting or important for the study of glassy materials (e.g., FA and slag). The Fe $L_{2,3}$-edge at ~710 eV falls in the energy range of COSMIC, whereas Fe $L_{2,3}$-edge XANES spectra of Fe—O coordination are only sensitive to the oxidation degree (Fe K-edge at ~7.1 keV is more sensitive to the local coordination changes [89–90]). Thus, Fe $L_{2,3}$-edge XANES spectra may be only applicable for Fe element mapping. The $L_{2,3}$-edge energy of potassium and Ca also falls in the designed beamline energy range. However, the minimum energy of the microscope is currently only optimized down to 500 eV. With the continuing optimization of the microscope, the STXM/ptychography will be applied into the full designed energy range (250–2500 eV). The X-ray beam at the Al and Si K-edge energy may only penetrate particle cement-related materials for up to ~15 μm. Over-sized particles would result in over-saturation in XANES spectra, limiting the detection of important absorption features and making data interpretations challenging. This transmission technique in two-dimensional mode may only characterize particles for a mixture of outer shells and inner products. STXM in the tomography mode can differentiate the outer and inner parts of each particle. However, this image stack data collection approach is not highly time-efficient due to the limited photon density from a third-generation synchrotron. The current minimum collection time for an 8 μm-by-8 μm area with one element of interest is ~1 h. The upgraded ALS, in few years, will emit a 100 times brighter beam than the current level. The data collection time would be significantly shortened, and even three-dimensional image stacks with XANES spectra can be collected in a reasonable timeframe.

4. Conclusions

In this paper, the use of STXM with ptychographic imaging at high soft X-ray energies (around Al and Si K-edge) has revealed the inter- and intra-particle spatial variations in the coordination environments of Al and Si of a Fe-rich fly ash sample. The different degrees of silicate polymerization and different coordination environments of Al among the fly ash particles have been visualized. The correlation between Al and Si coordination environments of fly ash aluminosilicate glass has been evidenced in the form of XANES spectra. Insufficient chemical information has been obtained from the direct SP/MAS NMR measurement due to the high paramagnetic Fe content in the FA sample. The peak shifts and width are largely affected by the paramagnetic element. The MQ/MAS NMR measurement can provide sufficient spectral resolution to peak deconvolution but is very time-consuming. Our improved XANES-based spectromicroscopic technique in the energy range of 1500–1850 eV is not limited by the paramagnetic ions in any sample or dense micron-sized particles (a limiting factor for low-energy ptychography imaging). This new spectromicroscopic characterization method is valuable for probing the local coordination environment of elements of interest in chemically heterogeneous poorly crystalline and glassy (supplementary) cementitious materials with a particle size of a few microns.

Supplementary data to this article can be found online at https://doi.org/10.1016/j.cemconres.2022.106947.

CRediT authorship contribution statement

Jiaqi Li: Conceptualization, Methodology, Investigation, Validation, Visualization, Writing – original draft, Funding acquisition. **Ke Xu:** Methodology, Validation, Visualization, Writing – original draft. **Guoqing Geng:** Methodology, Validation, Writing – review & editing. **Harris E. Mason:** Methodology, Investigation, Validation, Visualization, Writing – original draft, Supervision.

Declaration of competing interest

The authors declare that they have no known competing financial interests or personal relationships that could have appeared to influence the work reported in this paper.

Data availability

Data will be made available on request.

Acknowledgements

References

[1] P.J.M. Monteiro, S.A. Miller, A. Horvath, Towards sustainable concrete, Nat. Mater. 16 (2017) 698–699.

[2] S.A. Miller, R.J. Myers, Environmental impacts of alternative cement binders, Environ. Sci. Technol. 54 (2020) 677–686.

[3] M.C.G. Juenger, R. Snellings, S.A. Bernal, Supplementary cementitious materials: new sources, characterization, and performance insights, Cem. Concr. Res. 122 (2019) 257–273.

[4] I. Diaz-Loya, M. Juenger, S. Seraj, R. Minkara, Extending supplementary cementitious material resources: reclaimed and remediated fly ash and natural pozzolans, Cem.Concr.Compos. 101 (2019) 44–51.

[5] C. Shi, B. Qu, J.L. Provis, Recent progress in low-carbon binders, Cem. Concr. Res. 122 (2019) 227–250.

[6] G. Innocenti, D.J. Benkeser, J.E. Dase, X. Wirth, C. Sievers, K.E. Kurtis, Beneficiation of ponded coal ash through chemi-mechanical grinding, Fuel 299 (2021), 120892.

[7] ASTM, ASTM C618 Standard Specification for Coal Fly Ash And Raw Or Calcined Natural Pozzolan for Use in Concrete, 2019.

[8] P.T. Durdziński, C.F. Dunant, M.B. Haha, K.L. Scrivener, A new quantification method based on SEM-EDS to assess fly ash composition and study the reaction of its individual components in hydrating cement paste, Cem. Concr. Res. 73 (2015) 111–122.

[9] Q. Huang, X. Zhu, D. Liu, L. Zhao, M. Zhao, Modification of water absorption and pore structure of high-volume fly ash cement pastes by incorporating nanosilica, J. Build.Eng. 33 (2021), 101638.

[10] A. Palomo, S. Alonso, A. Fernandez-Jiménez, I. Sobrados, J. Sanz, Alkaline activation of fly ashes: NMR study of the reaction products, J. Am. Ceram. Soc. 87 (2004) 1141–1145.

[11] S.A. Bernal, J.L. Provis, B. Walkley, R. San Nicolas, J.D. Gehman, D.G. Brice, A. R. Kilcullen, P. Duxson, J.S. van Deventer, Gel nanostructure in alkali-activated binders based on slag and fly ash, and effects of accelerated carbonation, Cem. Concr. Res. 53 (2013) 127–144.

[12] S.L. Poulsen, V. Kocaba, G. Le Saoût, H.J. Jakobsen, K.L. Scrivener, J. Skibsted, Improved quantification of alite and belite in anhydrous Portland cements by 29Si MAS NMR: effects of paramagnetic ions, Solid State Nucl. Magn. Reson. 36 (2009) 32–44.

[13] S. Bae, C. Meral, J.-E. Oh, J. Moon, M. Kunz, P.J. Monteiro, Characterization of morphology and hydration products of high-volume fly ash paste by monochromatic scanning x-ray micro-diffraction(μ-SXRD), Cem. Concr. Res. 59 (2014) 155–164.

[14] L. Vincze, A. Somogyi, J. Osán, B. Vekemans, S. Török, K. Janssens, F. Adams, Quantitative trace element analysis of individual fly ash particles by means of X-ray microfluorescence, Anal. Chem. 74 (2002) 1128–1135.

[15] B. Walkley, J. Provis, Solid-state nuclear magnetic resonance spectroscopy of cements, Mater.Today Adv. 1 (2019), 100007.

[16] J. Li, G. Geng, W. Zhang, Y.S. Yu, D.A. Shapiro, P.J.M. Monteiro, The hydration of beta- and alpha(H)'-dicalcium silicates: an X-ray spectromicroscopic study, ACS Sustain. Chem. Eng. 7 (2019) 2316–2326.

[17] S. Bae, R. Taylor, D. Hernandez-Cruz, S. Yoon, D. Kilcoyne, P.J.M. Monteiro, Soft X-ray spectromicroscopic investigation of synthetic C-S-H and C3S hydration products, J. Am. Ceram. Soc. 98 (2015) 2914–2920.

[18] G. Geng, J. Li, Y.-S. Yu, D.A. Shapiro, D.A. Kilcoyne, P.J. Monteiro, Nanometer-resolved spectroscopic study reveals the conversion mechanism of CaO·Al2O3·10H2O to 2CaO·Al2O3·8H2O and 3CaO·Al2O3·6H2O at an elevated temperature, Cryst. Growth Des. 17 (2017) 4246–4253.

[19] G. Geng, R.J. Myers, Y.S. Yu, D.A. Shapiro, R. Winarski, P.E. Levitz, D.A. L. Kilcoyne, P.J.M. Monteiro, Synchrotron X-ray nanotomographic and

spectromicroscopic study of the tricalcium aluminate hydration in the presence of gypsum, Cem. Concr. Res. 111 (2018) 130–137.

[20] G.Q. Geng, R. Taylor, S. Bae, D. Hernandez-Cruz, D.A. Kilcoyne, A.H. Emwas, P.J. M. Monteiro, Atomic and nano-scale characterization of a 50-year-old hydrated C3S paste, Cem. Concr. Res. 77 (2015) 36–46.

[21] J. Li, W. Zhang, K. Xu, P.J.M. Monteiro, Fibrillar calcium silicate hydrate seeds from hydrated tricalcium silicate lower cement demand, Cem. Concr. Res. 137 (2020), 106195.

[22] G. Geng, R.J. Myers, A.L. Kilcoyne, J. Ha, P.J. Monteiro, Ca L2, 3-edge near edge X-ray absorption fine structure of tricalcium aluminate, gypsum, and calcium (sulfo) aluminate hydrates, Am. Mineral. 102 (2017) 900–908.

[23] J. Li, G. Geng, R. Myers, Y.S. Yu, D. Shapiro, C. Carraro, R. Maboudian, P.J. M. Monteiro, The chemistry and structure of calcium (alumino) silicate hydrate: a study by XANES, ptychographic imaging, and wide- and small-angle scattering, Cem. Concr. Res. 115 (2019) 367–378.

[24] P.J.M. Monteiro, G.Q. Geng, D. Marchon, J.Q. Li, P. Alapati, K.E. Kurtis, M.J. A. Qomi, Advances in characterizing and understanding the microstructure of cementitious materials, Cem. Concr. Res. 124 (2019), 105806.

[25] M. Abe, F. Kaneko, N. Ishiguro, T. Kudo, T. Matsumoto, T. Hatsui, Y. Tamenori, H. Kishimoto, Y. Takahashi, Development and application of a tender X-ray ptychographic coherent diffraction imaging system on BL27SU at SPring-8, J. Synchrotron Radiat. 28 (2021).

[26] R. Hoppe, J. Reinhardt, G. Hofmann, J. Patommel, J.-D. Grunwaldt, C. D. Damsgaard, G. Wellenreuther, G. Falkenberg, C.G. Schroer, High-resolution chemical imaging of gold nanoparticles using hard X-ray ptychography, Appl. Phys. Lett. 102 (2013), 203104.

[27] M. Rocca, Low-energy EELS investigation of surface electronic excitations on metals, Surf. Sci. Rep. 22 (1995) 1–71.

[28] J. Li, W. Zhang, C. Li, P.J.M. Monteiro, Eco-friendly mortar with high-volume diatomite and fly ash: performance and life-cycle assessment with regional variability, J. Clean. Prod. 261 (2020) 121224.

[29] D.A. Shapiro, S. Babin, R.S. Celestre, W. Chao, R.P. Conley, P. Denes, B. Enders, P. Enfedaque, S. James, J.M. Joseph, An ultrahigh-resolution soft X-ray microscope for quantitative analysis of chemically heterogeneous nanomaterials, Sci.Adv. 6 (2020), eabc4904.

[30] B. Vekemans, L. Vincze, F. Brenker, F. Adams, Processing of three-dimensional microscopic X-ray fluorescence data, J. Anal. At. Spectrom. 19 (2004) 1302–1308.

[31] M. Lerotic, C. Jacobsen, T. Schäfer, S. Vogt, Cluster analysis of soft X-ray spectromicroscopy data, Ultramicroscopy 100 (2004) 35–57.

[32] D.A. Shapiro, Y.-S. Yu, T. Tyliszczak, J. Cabana, R. Celestre, W. Chao, K. Kaznatcheev, A.D. Kilcoyne, F. Maia, S. Marchesini, Chemical composition mapping with nanometre resolution by soft X-ray microscopy, Nat. Photonics 8 (2014) 765–769.

[33] G. Hamerly, C. Elkan, Learning the k in k-means, Adv. Neural Inf. Proces. Syst. 16 (2004) 281–288.

[34] K. Krishna, M.N. Murty, Genetic K-means algorithm, IEEE Trans. Syst. Man Cybern. B Cybern. 29 (1999) 433–439.

[35] P.A. Bizopoulos, D.G. Tsalikakis, A.T. Tzallas, D.D. Koutsouris, D.I. Fotiadis, EEG epileptic seizure detection using k-means clustering and marginal spectrum based on ensemble empirical mode decomposition, in: 13th IEEE International Conference on Bioinformatics And Bioengineering, IEEE, 2013, pp. 1–4.

[36] A.F. Leontowich, R. Berg, C.N. Regier, D.M. Taylor, J. Wang, D. Beauregard, J. Geilhufe, J. Swirsky, J. Wu, C. Karunakaran, Cryo scanning transmission X-ray microscope optimized for spectrotomography, Rev. Sci. Instrum. 89 (2018), 093704.

[37] J. Yano, V.K. Yachandra, X-ray absorption spectroscopy, Photosynth. Res. 102 (2009) 241–254.

[38] F. De Groot, High-resolution X-ray emission and X-ray absorption spectroscopy, Chem. Rev. 101 (2001) 1779–1808.

[39] A. Hitchcock, P. Hitchcock, C. Jacobsen, C. Zimba, B. Loo, E. Rotenberg, J. Denlinger, R. Kneedler, aXis 2000—Analysis of X-ray Images And Spectra, McMaster University, Hamilton, ON, Canada, 2012.

[40] M.E. Wall, A. Rechtsteiner, L.M. Rocha, Singular value decomposition and principal component analysis, in: A Practical Approach to Microarray Data Analysis, Springer, 2003, pp. 91–109.

[41] S. Wold, K. Esbensen, P. Geladi, Principal component analysis, Chemom. Intell. Lab. Syst. 2 (1987) 37–52.

[42] E. Henry, J. Hofrichter, [8] singular value decomposition: application to analysis of experimental data, Methods Enzymol. 210 (1992) 129–192.

[43] R. Celestre, K. Nowrouzi, D.A. Shapiro, P. Denes, J.M. Joseph, A. Schmid, H. A. Padmore, Nanosurveyor 2: a compact instrument for nano-tomography at the advanced light source, in: Journal of Physics: Conference Series, IOP Publishing, 2017.

[44] M. Magi, E. Lippmaa, A. Samoson, G. Engelhardt, A. Grimmer, Solid-state high-resolution silicon-29 chemical shifts in silicates, J. Phys. Chem. 88 (1984) 1518–1522.

[45] J.-P. Amoureux, C. Fernandez, S. Steuernagel, ZFiltering in MQMAS NMR, J.Magn. Reson.Ser.A 123 (1996) 116–118.

[46] A. Goldbourt, P.K. Madhu, Multiple-quantum magic-angle spinning: high-resolution solid state NMR spectroscopy of half-integer quadrupolar nuclei, in: Current Developments in Solid State NMR Spectroscopy, 2002, pp. 17–54.

[47] D. Massiot, F. Fayon, M. Capron, I. King, S. Le Calvé, B. Alonso, J.O. Durand, B. Bujoli, Z. Gan, G. Hoatson, Modelling one-and two-dimensional solid-state NMR spectra, Magn. Reson. Chem. 40 (2002) 70–76.

[48] D. Li, G. Bancroft, M. Fleet, X. Feng, Y. Pan, Al K-edge XANES spectra of aluminosilicate minerals, 1995.

[49] D.R. Neuville, L. Cormier, D. Massiot, Al environment in tectosilicate and peraluminous glasses: a 27Al MQ-MAS NMR, Raman, and XANES investigation, Geochim. Cosmochim. Acta 68 (2004) 5071–5079.

[50] D.R. Neuville, L. Cormier, A.-M. Flank, V. Briois, D. Massiot, Al speciation and Ca environment in calcium aluminosilicate glasses and crystals by Al and Ca K-edge X-ray absorption spectroscopy, Chem. Geol. 213 (2004) 153–163.

[51] S. De Wispelaere, D. Cabaret, C. Levelut, S. Rossano, A.M. Flank, P. Parent, F. Farges, Na-, Al-, and Si K-edge XANES study of sodium silicate and sodium aluminosilicate glasses: influence of the glass surface, Chem. Geol. 213 (2004) 63–70.

[52] L. Andrini, R.M. Toja, M.S. Conconi, F.G. Requejo, N. Rendtorff, Halloysite nanotube and its firing products: structural characterization of halloysite, metahalloysite, spinel type silicoaluminate and mullite, J. Electron. Spectrosc. 234 (2019) 19–26.

[53] L. Andrini, M.R. Gauna, M.S. Conconi, G. Suarez, F.G. Requejo, E.F. Aglietti, N. Rendtorff, Extended and local structural description of a kaolinitic clay, its fired ceramics and intermediates: an XRD and XANES analysis, Appl. Clay Sci. 124 (2016) 39–45.

[54] D.R. Neuville, L. Cormier, D. Massiot, Al coordination and speciation in calcium aluminosilicate glasses: effects of composition determined by Al-27 MQ-MAS NMR and Raman spectroscopy, Chem. Geol. 229 (2006) 173–185.

[55] Z. Wu, C. Romano, A. Marcelli, A. Mottana, G. Cibin, G. Della Ventura, G. Giuli, P. Courtial, D. Dingwell, Evidence for Al/Si tetrahedral network in aluminosilicate glasses from Al K-edge X-ray-absorption spectroscopy, Phys. Rev. B 60 (1999) 9216.

[56] Q. Hu, M.T. Ley, J. Davis, J.C. Hanan, R. Frazier, Y. Zhang, 3D chemical segmentation of fly ash particles with X-ray computed tomography and electron probe microanalysis, Fuel 116 (2014) 229–236.

[57] D. Li, G.M. Bancroft, M.E. Fleet, X.H. Feng, Silicon K-edge Xanes spectra of silicate minerals, Phys. Chem. Miner. 22 (1995) 115–122.

[58] D. Li, G.M. Bancroft, M. Kasrai, M.E. Fleet, X.H. Feng, K.H. Tan, B.X. Yang, High-resolution Si K-edge and L2,3-edge Xanes of alpha-quartz and stishovite, Solid State Commun. 87 (1993) 613–617.

[59] J. Li, W. Zhang, K. Garbev, P.J. Monteiro, Coordination environment of Si in calcium silicate hydrates, silicate minerals, and blast furnace slags: a XANES database, Cem. Concr. Res. 143 (2021), 106376.

[60] G. Henderson, J. St-Amour, A Si K-edge XANES study of Ti containing alkali/alkaline-earth silicate glasses, Chem. Geol. 213 (2004) 31–40.

[61] X. Zhu, M. Zhang, K. Yang, L. Yu, C. Yang, Setting behaviours and early-age microstructures of alkali-activated ground granulated blast furnace slag (GGBS) from different regions in China, Cem. Concr. Compos. 114 (2020), 103782.

[62] K. Gong, E. Olivetti, Development of structural descriptors to predict dissolution rate of volcanic glasses: molecular dynamic simulations, 2021 arXiv preprint arXiv: 2107.14306.

[63] D. De Ligny, D. Neuville, L. Cormier, J. Roux, G. Henderson, G. Panczer, S. Shoval, A.-M. Flank, P. Lagarde, Silica polymorphs, glass and melt: an in situ high temperature XAS study at the Si K-edge, J. Non-Cryst. Solids 355 (2009) 1099–1102.

[64] Y. Chen, N. Shah, F. Huggins, G. Huffman, A. Dozier, Characterization of ultrafine coal fly ash particles by energy-filtered TEM, J. Microsc. 217 (2005) 225–234. Oxford.

[65] C. Romano, E. Paris, B.T. Poe, G. Giuli, D.B. Dingwell, A. Mottana, Effect of aluminum on Ti-coordination in silicate glasses: a XANES study, Am. Mineral. 85 (2000) 108–117.

[66] D. Li, in: Aluminum, Silicon, Phosphorus And Sulfur K-And L-edge X-ray Absorption Spectroscopy Of Minerals And Glasses: Applications In Mineralogy And Geochemistry, 1994, p. 2432. PhD thesis.

[67] Y. Wang, S. Luo, L. Yang, Y. Ding, Microwave curing cement-fly ash blended paste, Constr. Build. Mater. 282 (2021), 122685.

[68] C. Ruiz-Santaquiteria, J. Skibsted, A. Fernández-Jiménez, A. Palomo, Alkaline solution/binder ratio as a determining factor in the alkaline activation of aluminosilicates, Cem. Concr. Res. 42 (2012) 1242–1251.

[69] F. Bonk, J. Schneider, M.A. Cincotto, H. Panepucci, Characterization by multinuclear high-resolution NMR of hydration products in activated blast-furnace slag pastes, J. Am. Ceram. Soc. 86 (2003) 1712–1719.

[70] G. Fang, M. Zhang, Multiscale micromechanical analysis of alkali-activated fly ash-slag paste, Cem. Concr. Res. 135 (2020), 106141.

[71] X. Gao, Q. Yu, H. Brouwers, Apply 29Si, 27Al MAS NMR and selective dissolution in identifying the reaction degree of alkali activated slag-fly ash composites, Ceram. Int. 43 (2017) 12408–12419.

[72] Z. Peng, K. Vance, A. Dakhane, R. Marzke, N. Neithalath, Microstructural and 29Si MAS NMR spectroscopic evaluations of alkali cationic effects on fly ash activation, Cem. Concr. Compos. 57 (2015) 34–43.

[73] S. Greiser, G.J. Gluth, P. Sturm, C. Jäger, 29 Si 27 Al}, 27 Al {29 Si and 27 Al 1 H double-resonance NMR spectroscopy study of cementitious sodium aluminosilicate gels (geopolymers) and gel–zeolite composites, RSC Adv. 8 (2018) 40164–40171.

[74] L. Kriskova, Y. Pontikes, Ö. Cizer, A. Malfliet, J. Dijkmans, B. Sels, K. Van Balen, B. Blanpain, Hydraulic behavior of mechanically and chemically activated synthetic merwinite, J. Am. Ceram. Soc. 97 (2014) 3973–3981.

[75] D. Bonenfant, L. Kharoune, S. Sauve, R. Hausler, P. Niquette, M. Mimeault, M. Kharoune, CO2 sequestration potential of steel slags at ambient pressure and temperature, Ind. Eng. Chem. Res. 47 (2008) 7610–7616.

[76] J.F. Stebbins, K.E. Kelsey, Anomalous resonances in 29 Si and 27 Al NMR spectra of pyrope ([Mg, Fe] 3 Al 2 Si 3 O 12) garnets: effects of paramagnetic cations, Phys. Chem. Chem. Phys. 11 (2009) 6906–6917.

[77] J.F. Stebbins, W.R. Panero, J.R. Smyth, D.J. Frost, Forsterite, wadsleyite, and ringwoodite (Mg2SiO4): 29Si NMR constraints on structural disorder and effects of paramagnetic impurity ions, Am. Mineral. 94 (2009) 626–629.

[78] A.C. Palke, J.F. Stebbins, D.J. Frost, C.A. McCammon, Incorporation of Fe and Al in MgSiO3 perovskite: an investigation by 27Al and 29Si NMR spectroscopy, Am. Mineral. 97 (2012) 1955–1964.

[79] A.C. Palke, J.F. Stebbins, Variable-temperature 27Al and 29Si NMR studies of synthetic forsterite and Fe-bearing Dora Maira pyrope garnet: temperature dependence and mechanisms of paramagnetically shifted peaks, Am. Mineral. 96 (2011) 1090–1099.

[80] H.-I. Kim, J.C. Sur, S.K. Lee, Effect of iron content on the structure and disorder of iron-bearing sodium silicate glasses: a high-resolution 29Si and 17O solid-state NMR study, Geochim. Cosmochim. Acta 173 (2016) 160–180.

[81] A. Schöler, F. Winnefeld, M.B. Haha, B. Lothenbach, The effect of glass composition on the reactivity of synthetic glasses, J. Am. Ceram. Soc. 100 (2017) 2553–2567.

[82] H. Maraghechi, F. Rajabipour, C.G. Pantano, W.D. Burgos, Effect of calcium on dissolution and precipitation reactions of amorphous silica at high alkalinity, Cem. Concr. Res. 87 (2016) 1–13.

[83] K.C. Newlands, M. Foss, T. Matchei, J. Skibsted, D.E. Macphee, Early stage dissolution characteristics of aluminosilicate glasses with blast furnace slag-and fly-ash-like compositions, J. Am. Ceram. Soc. 100 (2017) 1941–1955.

[84] K.L. Aughenbaugh, P. Stutzman, M.C.G. Juenger, Identifying glass compositions in fly ash, Front. Mater. 3 (2016).

[85] A. Gianoncelli, G. Kourousias, L. Merolle, M. Altissimo, A. Bianco, Current status of the TwinMic beamline at Elettra: a soft X-ray transmission and emission microscopy station, J. Synchrotron Radiat. 23 (2016) 1526–1537.

[86] H.-J. Shin, N. Kim, H.-S. Kim, W.-W. Lee, C.-S. Lee, B. Kim, A scanning transmission X-ray microscope at the Pohang Light Source, J. Synchrotron Radiat. 25 (2018) 878–884.

[87] Z. Xu, C. Wang, H. Liu, X. Tao, R. Tai, Low-dose, high-resolution and high-efficiency ptychography at STXM beamline of SSRF, in: Journal of Physics: Conference Series, IOP Publishing, 2017.

[88] J.C. da Silva, C. Guilloud, O. Hignette, C. Jarnias, C. Ponchut, M. Ruat, J.-C. Labiche, A. Pacureanu, Y. Yang, M. Salome, Overcoming the challenges of high-energy X-ray ptychography, J. Synchrotron Radiat. 26 (2019) 1751–1762.

[89] B. Ma, A. Fernandez-Martinez, K. Wang, B. Madé, P. Hénocq, D. Tisserand, S. Bureau, L. Charlet, Selenite sorption on hydrated CEM-V/A cement in the presence of steel corrosion products: redox vs nonredox sorption, Environ. Sci. Technol. 54 (2020) 2344–2352.

[90] B. Ma, A. Fernandez-Martinez, B. Made, N. Findling, E. Markelova, E. Salas-Colera, T.G.G. Maffeis, A.R. Lewis, D. Tisserand, S. Bureau, L. Charlet, XANES-based determination of redox potentials imposed by steel corrosion products in cement-based media, Environ. Sci. Technol. 52 (2018) 11931–11940.